



# **JGR** Earth Surface

### RESEARCH ARTICLE

10.1029/2023JF007389

#### **Key Points:**

- Channel dimensions are the dominant factor controlling the occurrence and strength of the rip current
- The channel evolution is affected by both the initial channel dimensions and the wave conditions
- The spatial distribution of rip current forcings and the relative importance of terms depend on the channel dimensions

#### Correspondence to:

D. F. Christensen, dc@ign.ku.dk

#### Citation:

Christensen, D. F., Raubenheimer, B., & Elgar, S. (2024). The roles of bathymetry and waves in rip-channel dynamics. Journal of Geophysical Research: Earth Surface, 129, e2023JF007389. https://doi.org/10.1029/2023JF007389

Received 16 AUG 2023 Accepted 19 DEC 2023

## The Roles of Bathymetry and Waves in Rip-Channel Dynamics

D. F. Christensen<sup>1,2</sup>, B. Raubenheimer<sup>2</sup>, and S. Elgar<sup>2</sup>

<sup>1</sup>Department of Geosciences and Natural Resource Management, University of Copenhagen, Copenhagen K, Denmark, <sup>2</sup>AOPE Department, Woods Hole Oceanographic Institution, Woods Hole, MA, USA

**Abstract** The behavior and predictability of rip currents (strong, wave-driven offshore-directed surfzone currents) have been studied for decades. However, few studies have examined the effects of rip channel morphology on the rip generation or have compared morphodynamic models with observations. Here, simulations conducted with the numerical morphodynamic model MIKE21 reproduce observed trends in flows and bathymetric evolution for two channels dredged across a nearshore sandbar and terrace on an ocean beach near Duck, NC, USA. Channel dimensions, wave conditions, and flows differed between the two cases. In one case, a strong rip current was driven by moderate height, near-normally incident waves over an approximately 1-m deep channel with relatively little bathymetric evolution. In the other case, no rip was generated by the large, near-normally incident waves over the shallower ( $\sim 0.5$  m) channel, and the channel migrated in the direction of the mean flow and eventually filled in. The model simulated the flow directions, the generation (or not) of rip currents, and the morphological evolution of the channels reasonably well. Model simulations were then conducted for different combinations of the two channel geometries and two wave conditions to examine the relative importance of the waves and morphology to the rip current evolution. The different bathymetries were the dominant factor controlling the flow, whereas both the initial morphology and wave conditions were important for channel evolution. In addition, channel dimensions affected the spatial distribution of rip current forcings and the relative importance of terms.

Plain Language Summary Rip currents are strong offshore-directed currents that form on beaches worldwide where they pose a major risk to beachgoers. Despite rip currents being studied for decades, the influence of the seafloor shape on rip current generation and strength remains uncertain. Here we use a numerical model to simulate flows and evolution of the seafloor for two rip currents observed on a sandy beach near Duck, NC, USA. The model successfully reproduced the observed trends and was used to investigate the rip current forcing mechanisms for different seafloor shapes and wave conditions. The seafloor configuration was found to be the dominant factor controlling rip current generation. A 1-m deep channel created a stronger and more persistent rip current compared with a 0.5-m deep channel during similar wave conditions. The rip currents were primarily driven by alongshore differences in water level with a local minimum within the channel. The water levels forced two converging shore-parallel "feeder" currents transporting water into the offshore-directed rip current. Moreover, waves changed direction over the deep channel, resulting in higher wave energy on the channel sides and lower energy in the channel center. Alongshore variations in wave heights thereby modulated the strength of the feeders.

#### 1. Introduction

Channel rips are strong, wave-driven offshore-directed surfzone currents associated with alongshore bathymetric variability. Rip current strengths typically are of the order of 0.5 m/s, but can exceed 2 m/s during storms (Houser et al., 2020), and pose a major risk for beachgoers (Brander, 2015). In addition, rips are important for the exchange of sediments, nutrients, pollutants, phytoplankton, and fish larvae across the surf zone (Aagaard et al., 1997; Brown et al., 2009, 2015; Fujimura et al., 2014; Gallop et al., 2018; MacMahan et al., 2010; Reniers et al., 2009). Channel rips are associated with intermediate beach types (following the classification by Wright and Short (1984)) that are characterized by a rhythmic nearshore morphology, often involving rip channels incising a bar-trough or terraced beach (Dalrymple et al., 2010). The momentum balance for the forcing of the two converging alongshore-directed feeder currents that transport water into the offshore-directed rip current is given by Haller et al. (2002) and Kumar et al. (2011):

© 2024. American Geophysical Union. All Rights Reserved.

CHRISTENSEN ET AL. 1 of 15

$$\underbrace{C_d \sqrt{U^2 + V^2} V}_{\text{Feeder}} \sim \underbrace{gh \frac{\partial \eta}{\partial y}}_{\text{Setup}} + \underbrace{\frac{\partial S_{yy}}{\partial y} + \frac{\partial S_{xy}}{\partial x}}_{\text{Radiation}} + \underbrace{hU \frac{\partial V}{\partial x} + hV \frac{\partial V}{\partial y}}_{\text{Advection}}$$

$$\underbrace{\text{Setup}}_{\text{gradients}} \times \text{Radiation} \times \text{Stresses}$$

$$(1)$$

Here  $C_d$  is the drag coefficient, U and V are the cross- (x-direction) and alongshore (y-direction) flow velocities, g the gravitational acceleration, h the total mean water depth,  $\eta$  the wave-driven setup (h- $\eta$  = still water depth), and  $S_{yy}$  and  $S_{xy}$  the alongshore and diagonal components of the radiation stress, respectively. With increasing wave heights, wave breaking may become stronger on the shallow sides of the channel and force larger setups, resulting in stronger feeders and increased rip current velocity (MacMahan et al., 2006; Winter et al., 2014). Rip behavior and predictability have been studied for decades (Shepard, 1936). However, owing to the difficulties related to a priori locating rips on natural beaches and deploying instruments within the short time frame (hours to days) of rip current presence, field observations of rip currents often have relatively small spatial and temporal coverage (see MacMahan et al. (2006), Table 1). Thus, many laboratory experiments over a range of beach morphologies have been conducted to facilitate investigations of the flow dynamics (Castelle et al., 2010; Haas & Svendsen, 2002; Haller et al., 2002; Kennedy et al., 2008; Kennedy & Thomas, 2004).

Numerical models reproduce the observed trends in the occurrence, strength, and persistence of channel rip currents for variable wave conditions (Bruneau et al., 2011; Hu et al., 2022; Kumar et al., 2011; Marchesiello et al., 2015; Reniers et al., 2009; Schmidt et al., 2005; Winter et al., 2014). Numerical studies examining flow and bathymetry interactions have focused on predicting rip spacing (Calvete, 2005; Damgaard et al., 2002; Deigaard et al., 1999; Reniers et al., 2004; Valipour & Bidokhti, 2018), and the dependence of rip currents on channel dimensions (Brander, 1999; Castelle et al., 2010; Hong et al., 2021; Kennedy et al., 2008; McCarroll et al., 2018; Winter 2012). However, the bathymetric effects on rip generation and strength remain uncertain, and there are few field and corresponding numerical investigations of sediment transport and channel evolution (Houser et al., 2020).

Here, simulations of rip channel hydrodynamics and morphological evolution using the numerical model MIKE21 (DHI, 2020) show similar trends as field observations in channels dredged across a surf zone (Section 3). The model is used to investigate the forces driving rip currents for different bathymetries and wave conditions (Section 4).

## 2. Field Study and Model Setup

#### 2.1. Field Site, Data Collection, and Wave Conditions

A field experiment (Moulton et al., 2017) was conducted between 27 June and 7 August 2012 at the US Army Corps of Engineers Field Research Facility (FRF) on the Outer Banks, near Duck, NC, USA (Figure 1).

The beach is intermediate (Wright & Short, 1984) with shore-normal orientation 72°N. During the experiment, the nearshore bathymetry changed between a terrace and a small alongshore bar (0.5–1.0 m from trough to crest). Shore-perpendicular channels were excavated across the terrace or nearshore bar on July 8 (Jul8, Figures 2a and 2c) and July 20 (Jul20, Figures 2b and 2d) with initial depths of 0.5–1.0 m and widths of 20–40 m.

The channels and the surrounding bathymetry were surveyed using a jet ski with surveying equipment (Moulton et al., 2014). The initial Jul20 channel is approximately twice the width of the Jul8 bathymetry (cross-shore coordinate 130 m) and extends farther offshore across an inner bar (Figure 3). Surveys were performed daily except during large waves, including at the beginning and end (3–10 days later) of each channel experiment.

Incident (26-m water depth) significant wave heights ( $H_s$ ) ranged from 0.5 to 1.6 m, periods ( $T_m$ ) between 5 and 9 s, and directions (MWD) from 65 to 200°N (Figure 4). Tides are semi-diurnal and the average tidal range was 1 m. Nearshore water levels, wave heights, and currents were measured at 2 Hz in and near the channels with bottom mounted, colocated pressure sensors and Acoustic Doppler Velocimeters (ADVs) (Figures 2a and 2b). The ADVs were oriented to measure positive flows to the north and offshore.

CHRISTENSEN ET AL. 2 of 15

21699011, 2024, 1, Downloaded from https://agupubs.onlinelibrary.wiley.com/doi/10.1029/2023JR007389 by Mbl Whoi Library. Wiley Online Library on [04/01/2024]. See the Terms and Condition

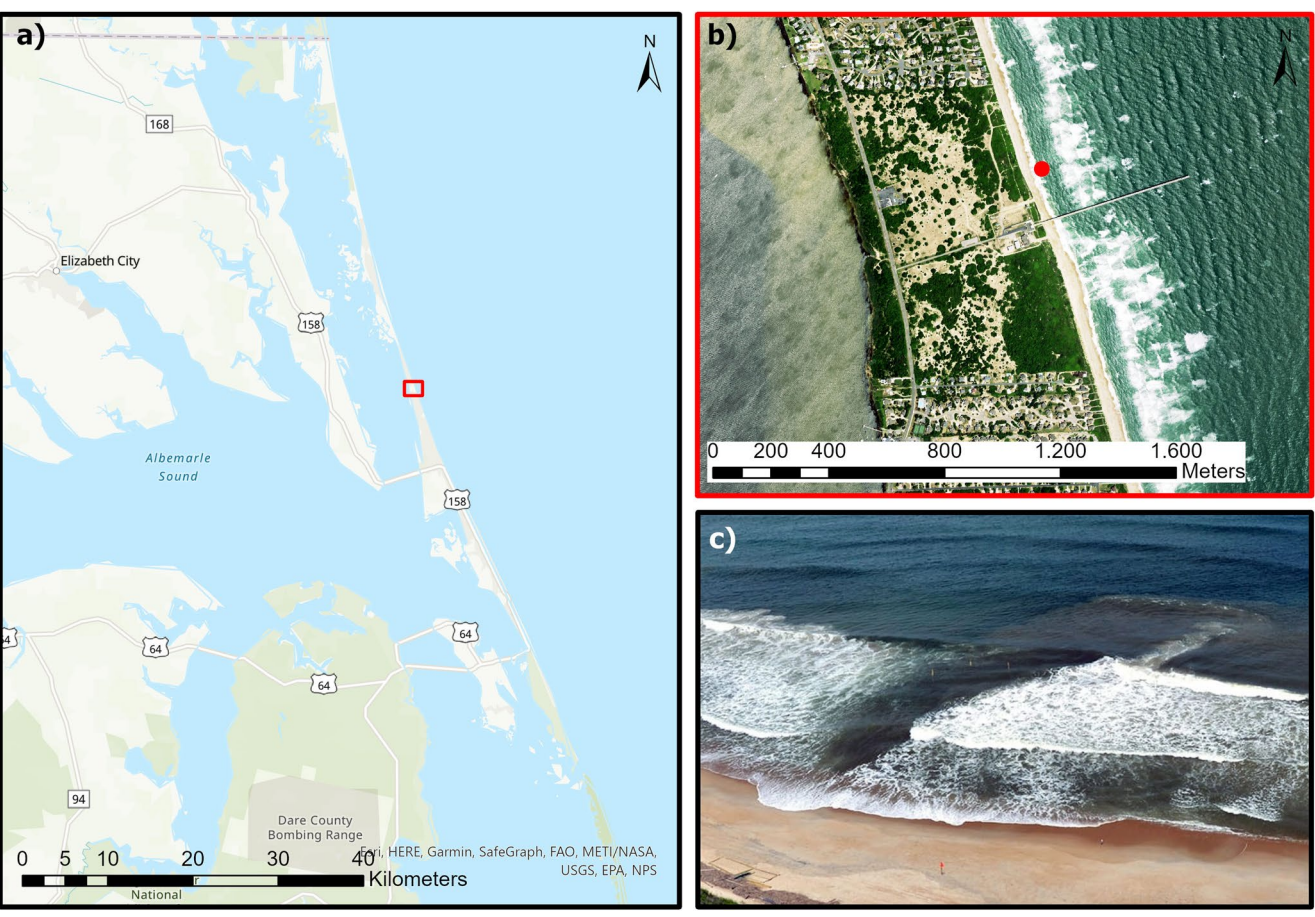


Figure 1. Overview map of north-eastern North Carolina, USA (a) with the red rectangle showing the field location of the Field Research Facility in Duck, NC, (b) an orthophoto of the field site (OCM Partners, 2023) with the red dot indicating the location of the July 20 dredged channel, and (c) photo of a rip current in a dredged channel (by Melissa Moulton).

## 2.2. Model Description and Configuration

As in many prior rip current studies (Bruneau et al., 2011; Hu et al., 2022; Schmidt et al., 2005; Winter et al., 2014), a depth- and phase-averaged (two-dimensional) model is used here owing to the computational costs of fully 3D or phase-resolved models. In addition, few 3D or phase-resolved models include fully coupled surfzone waves and hydrodynamics, and morphological changes. The depth- and phase-averaged numerical model used here, MIKE21 Flexible Mesh, consists of three modules: Spectral Wave (SW), Hydrodynamic (HD), and Sand Transport (ST), which can be coupled to simulate the interactions between waves, currents, and morphology (DHI, 2017a, 2017b, 2020). The MIKE modeling system simulates shallow-water processes over complex bathymetry (Osorio-Cano et al., 2019; Warren & Bach, 1992). However, few surfzone studies have included the ST module (Badru et al., 2022; Cáceres et al., 2016; Petropoulos et al., 2022; Valipour & Bidokhti, 2018; Valipour et al., 2014) or compared the model with field measurements of morphological changes. The SW module simulates the wave transformation based on either a fully spectral (FS) or directional decoupled (DD) formulation solving the wave action conservation equation (Komen et al., 1994) or a parameterization hereof (Holthuijsen et al., 1989). The DD formulation is used here and solved using a stationary solution. Simulated wave radiation stresses are used as an input in the HD module where Reynolds averaged Navier-Stokes equations are solved using an in-stationary solution to simulate wave-induced currents. The combined action of waves and currents on sediment mobilization and transportation as bed load and suspended load is calculated in the ST module using a quasi-3D look-up table. This pre-generated table must consist of any waves and currents predicted by the SW and HD modules as well as sediment conditions. Sediment transport rates are found by linear interpolations in the table, and subsequently used to simulate bed-level changes by solving the continuity equation (DHI, 2020). The finite volume method is used to solve the equations of the three modules in MIKE21.

CHRISTENSEN ET AL. 3 of 15

21699011, 2024, 1, Downloaded from https://agupubs.onlinelibrary.wiley.com/doi/10.1029/2023JH007389 by Mbl Whoi Library, Wiley Online Library on [04/01/2024]. See the Terms and Conditions (https://onlinelibrary

ons) on Wiley Online Library for rules of use; OA articles are governed by the applicable Creative Commons Licens

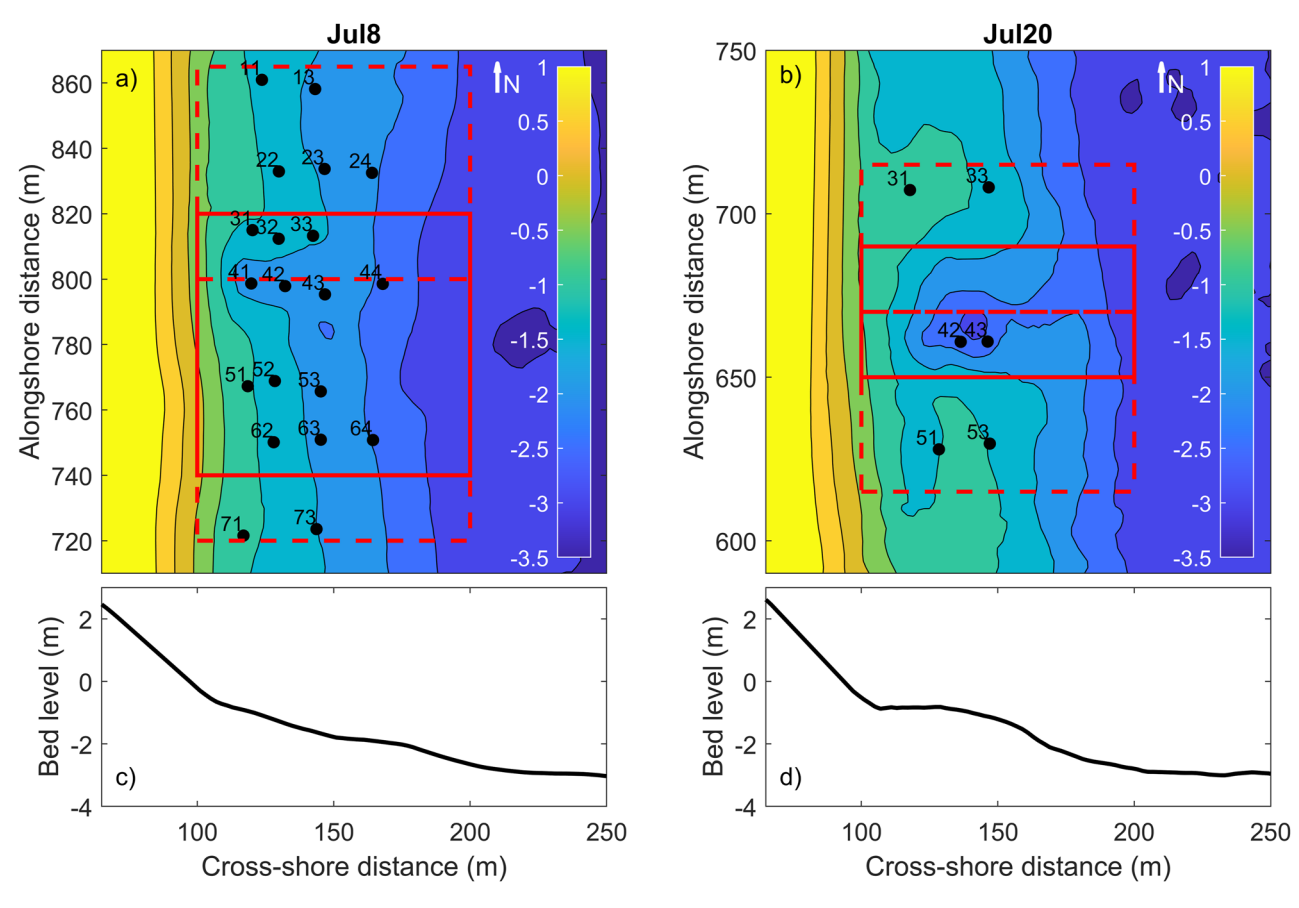


**Figure 2.** (a and b) Initial bathymetry (color contours, scale on right, with contour curves every 0.5 m) as a function of alongshore and cross-shore distance (north and offshore to the top and right, respectively) with instrument positions as black dots. Red rectangles define regions for the estimation of characteristic flow velocities (dashed lines for feeders on channel sides, and solid lines for the rip current in the channel center), and bed-level elevations (relative to NAVD88) versus cross-shore distance at alongshore distance (c) 850 m (Jul8) and (d) 710 m (Jul20).

Varying triangular cell sizes were used across the study area. In the area of interest (+600 m north and south of the channel center and 800 m in the cross-shore direction), the maximum cell size is 8 m. In the rest of the domain, which covers 5,200 m alongshore and 1,000 m cross-shore, cell sizes vary between approximately 20 and 144 m (getting coarser away from the channel in both directions). The mesh consists of a total of 62,157 triangular cells. Bed-level data were applied to the mesh using linear interpolation. The bathymetric information

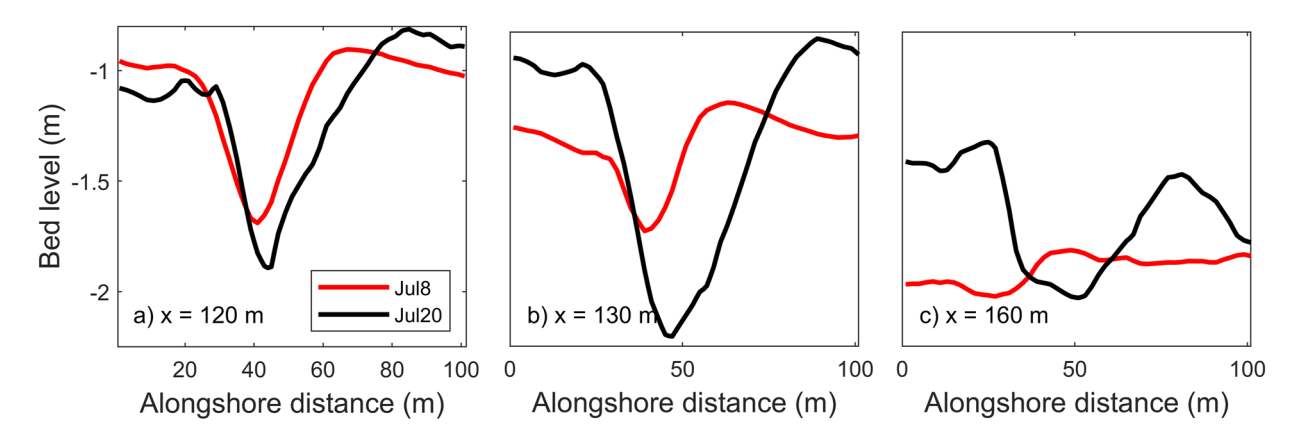


Figure 3. Bed level (depth relative to NAVD88) versus alongshore distance at cross-shore location (a) 120 m, (b) 130 m, and (c) 160 m during Jul8 (red) and Jul20 (black).

CHRISTENSEN ET AL. 4 of 15



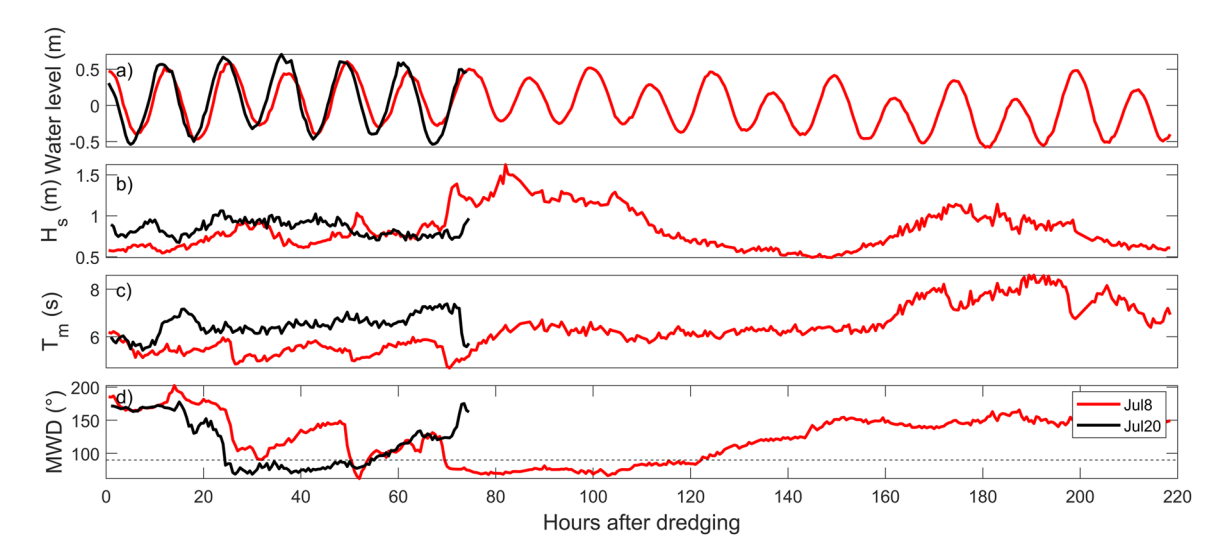


Figure 4. (a) Tidal elevation, (b) significant wave height  $(H_s)$ , (c) mean wave period  $(T_m)$ , and (d) mean wave direction (MWD) observed in 26-m water depth versus time (hours since channel dredging) during Jul8 (red) and Jul20 (black). The dashed line in (d) is the direction of shore-normal.

consisted of three different data sets: a regional DEM based on a combination of a NOAA and a North Carolina DEM, a local FRF property DEM based on data collected from the Lighter Amphibious Resupply Cargo (LARC) on 27 June 2012, and the site-specific jet ski surveys on July 8 and 20, 2012. Information on water levels (Flather condition) and wave conditions were given along the offshore boundary, while the lateral boundaries were closed.

The model was run with minimum solution time steps of 0.01 s to satisfy a Courant-Friedrichs-Lewy criterion of 0.8. The overall time step at which the three modules are synchronized and simulated output saved was 1800 s. The wave action conservation equation was solved using 72 directional bins of  $5^{\circ}$ . Wave-current interaction was excluded because it resulted in occasional high, erroneous wave heights. This omission caused minimal effects on the rip and feeder flow velocities. Different gamma (ratio of significant wave height to water depth) specifications were tested for the simulation of the depth-limited wave breaking. Based on the best fit of the modeled wave heights with those observed during Jul20 (RMSE = 0.11 m), a constant gamma of 0.45 was used. A low bed roughness (Chezy =  $52 \text{ m}^{1/2}$ /s) and eddy viscosity of  $0.05 \text{ m}^2$ /s (similar to Moulton et al. (2017)) was applied in the HD module. Sediment properties were  $D50 = 200 \,\mu\text{m}$  and a grading coefficient of 1.51 based on sediment samples collected at Duck in 2018-2021. Defaults were used for the remaining model parameters.

Depth-averaged models often underestimate rip current flow velocities, likely owing to neglecting three-dimensional effects (Marchesiello et al., 2015). Furthermore, although time-averaging may result in reasonable large-scale behavior (Zhang et al., 2022), small-scale hydrodynamics (and feedbacks with bathymetry) must be parameterized, possibly also contributing to underestimation of bathymetric changes. The simulated erosion and deposition volumes were multiplied by a factor (morph-fac) at every time step to obtain realistic morphological changes given the underestimation of undertow and rip currents. To reproduce the observed average (over the entire study area) sand-level changes between the start and end of each channel study, a factor of 5 was used for the Jul8 channel and a factor of 2 for the Jul20 study (a detailed sensitivity study was not undertaken to hone these factors).

#### 3. Model-Data Comparison

Simulated flows are variable in time, with rip flow maxima shifting position within the channel. As in prior studies (Moulton et al., 2017), characteristic flow velocities are defined as the maximum offshore- or alongshore-directed (toward the channel center) flows within regions. If the maximum alongshore flow velocities toward the channel center did not exceed 0.1 m/s, the maximum flow velocity in the wave propagation direction was used (Moulton et al., 2017). During Jul20, the channel position was roughly constant at alongshore position 670 m (at cross-shore coordinate 130 m) and the regions for extracting maximum current velocities are defined as a) the channel center at alongshore coordinate 670 m  $\pm$  20 m (Figure 2b, regions defined by solid red rectangle)

CHRISTENSEN ET AL. 5 of 15

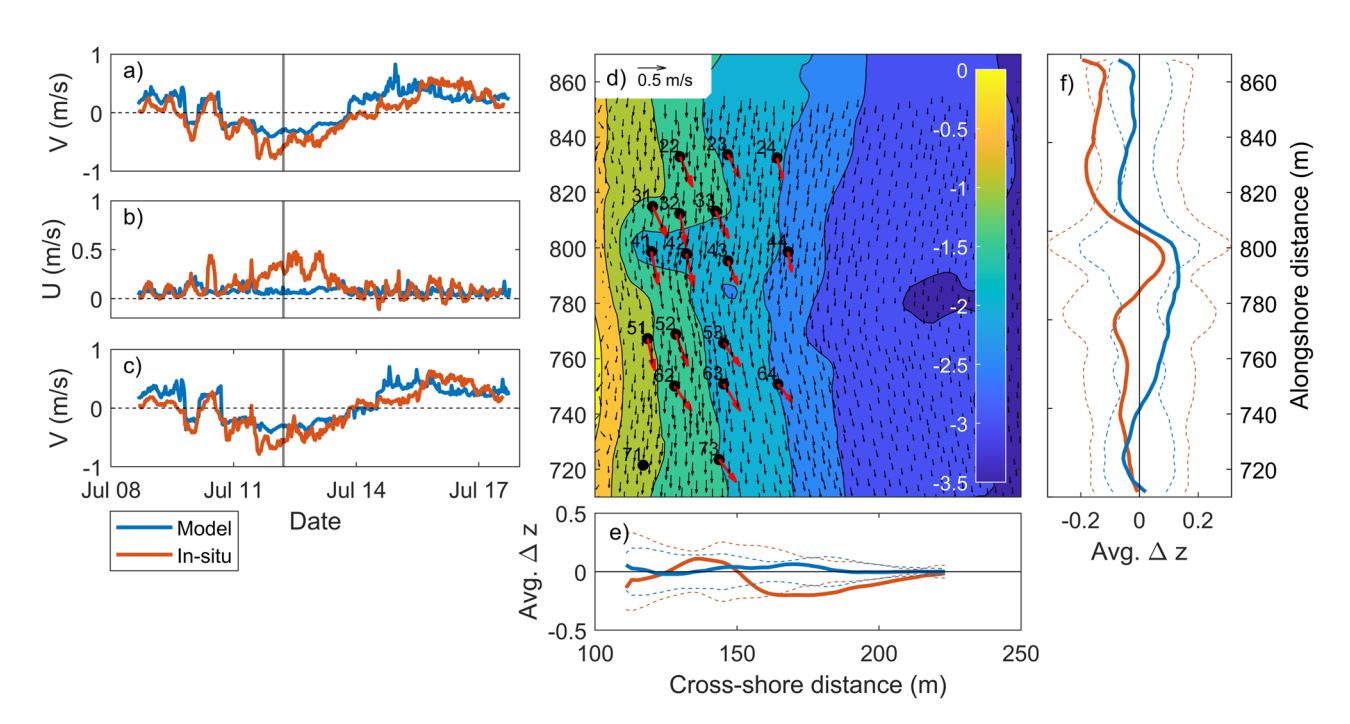


Figure 5. (a, c) Alongshore and (b) cross-shore flows versus time, (d) initial bathymetry as a function of alongshore and cross-shore distance with arrows representing time-averaged flows during hour 85 (in black depth-averaged model results and in red in-situ measurements), and average (over 710 < y < 870 m, and 110 < x < 225 m, solid curves) and  $\pm$  1std (dashed curves) bed-level changes between July 8 and 17 July 2012 versus (e) cross- and (f) alongshore distance. In panels (a–c, e, and f), the orange curves are observations and the blue curves are model simulations. The vertical gray bars in panel (a–c) are drawn at hour 85.

and b) 50 m to the north and south of the center (Figure 2b, areas with dashed red rectangles), with all regions spanning cross-shore coordinates 100–200 m. The channel location evolved during Jul8, with an alongshore position of 798 m on July 8-10, shifting to the south on July 13 (alongshore position 764 m), and back north on July 17 (alongshore position 824 m) (all positions are at cross-shore coordinate 130 m). Larger regions were therefore defined for the rip (alongshore coordinate 740–820 m) and feeder currents (alongshore coordinate 800–860 and 720–800 m, Figure 2a). Instruments 51–53 and 62–64 (Figure 2a) are used either for feeder (beginning and end of the experiment) or rip current (mid experiment) velocities as they are encompassed by both regions.

Model-data comparisons of the morphological changes between the time of the initial and end surveys are made by averaging the bed-level changes over the cross-shore (cross-shore coordinate 100-250 m) or alongshore (Jul8: 740-860 m, Jul20: 610-730 m).

The coupled MIKE21 model reproduces the trends in flow behavior and morphological changes during the experiments (Figures 5 and 6). Both measured and simulated flows show dominance of an alongshore current to the south during Jul8 (Figures 5a, 5c, and 5d), whereas a strong rip current was present from noon July 21 until late evening July 23, with converging alongshore feeder currents (Figures 6a and 6c) and strong offshore flows in the rip channel (Figure 6b). The alongshore feeder flows are well reproduced by the model, with root-mean-square errors normalized by the flow range (nrms = 0.15 on the north side, and nrms = 0.20 on the south side) similar to those in prior comparisons with the COAWST model (Moulton et al., 2017). Similar to prior studies with 2D models (Bruneau et al., 2011), rip flow velocities are underestimated. Prior studies (Marchesiello et al., 2015) have suggested that rip velocities may be enhanced by coupling between the 2D and 3D dynamics, which are neglected here. In particular, neglecting the exchange of momentum between vertically sheared flows and the depth-averaged flows may cause an underestimation of the rip cell recirculation and overestimation of the bottom stresses. In addition, vertical flow shear with near-bottom rip flow maxima may result in discrepancies between the in situ point measurements and the depth-averaged simulations, and wave-phase averaging in the model may result in an underestimation of the rip forcing (Kumar et al., 2011).

Average bed-level changes are also comparable for the observations and simulations (Figures 6e and 6f). Sediment is deposited within the channels during both experiments (Figures 5f and 6f, averaged  $\Delta z$  near the channel center >0, where z is vertical elevation). During Jul20, bed-level changes were small north and south of the

CHRISTENSEN ET AL. 6 of 15

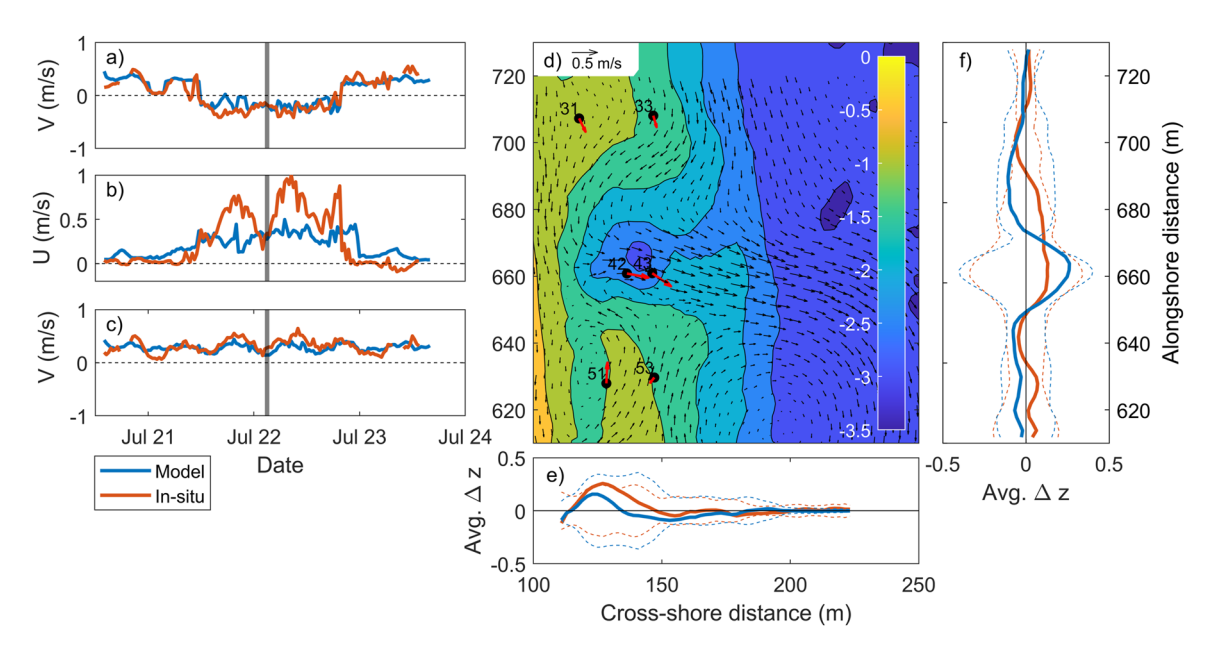


Figure 6. (a, c) Alongshore and (b) cross-shore flows versus time, (d) initial bathymetry as a function of alongshore and cross-shore distance with arrows representing time-averaged flows during hour 37 (in black depth-averaged model results and in red in-situ measurements), and average (over 610 < y < 730 m, and 110 < x < 225 m, solid curves) and  $\pm$  1std (dashed curves) bed-level changes between July 20 and 23 July 2012 versus (e) cross- and (f) alongshore distance. In panels (a–c, e, and f), the orange curves are observations and the blue curves are model simulations. The vertical gray bars in panels (a–c) are drawn at hour 37.

channel (Figure 6f). However, during Jul8, erosion was observed and modeled over the north side of the channel (which initially was relatively shallow) (Figures 5f, 810 < alongshore coordinate < 840 m). The average bed-level changes were variable during Jul8 (Figure 7a). Near the channel midpoint (at cross-shore coordinate 130 m) the Jul8 bathymetry was observed (orange dashed curve) and modeled (blue dashed curve) to accrete on the northern channel side between July 10 and 13 (compare dotted and dashed lines), while the channel was displaced to the south. Deposition volumes are underestimated by the model despite the morph-fac, but the model reproduces the channel infilling (between alongshore coordinate 780 and 820 m) and the alongshore displacement of the channel (lowest bed level near alongshore coordinate 765 m). Subsequently, both observations and model results show an infilling of the new southern channel (between alongshore coordinate 750 and 780 m). Simultaneously, the observed deposited material in the northern part eroded, resulting in a lower than initial bed level corresponding to the model results (between alongshore coordinate 810 and 840 m). During Jul20 (Figure 7b), moderate channel infilling and narrowing occurred (both modeled and observed deposition between alongshore position 650–670 m). The model simulates erosion on the northern channel slope (between alongshore position 670–700 m) causing a shift in the channel position, which was not in accordance with field observations.

#### 4. Rip Current Dynamics

To examine whether the differences in the rip generation for Jul8 and Jul20 are primarily due to the differences in the bathymetries or the wave climate, simulations are conducted for combined cases of Jul8 and Jul20 waves and bathymetries (Figure 8). Hence, "combined case Jul8" (CC-Jul8) is a simulation based on the Jul8 bathymetry with the Jul20 wave conditions and a morph-fac of 2. The "combined case Jul20" (CC-Jul20) is a simulation based on the Jul20 bathymetry with the Jul8 wave conditions and a morph-fac of 5. The choice of morph-fac did not significantly alter the morphological evolution (<0.05 m differences in channel depths were observed if applying a factor 5 instead of 2 in CC-Jul8).

The combined cases indicate that the observed and modeled flow differences between Jul8 and Jul20 are primarily related to the different bathymetries and not the wave conditions. Comparing Jul8 with CC-Jul8 (same bathymetry, different waves), flows on the channel sides are unidirectional for Jul8 (Figure 8, solid red curves), whereas for CC-Jul8, there is flow convergence at low tides between hour 20 to 56 when waves were near normally incident (Figures 8a and 8c see dotted red curve for the period highlighted by red arrows). However, the offshore-directed flows within the channel are somewhat weaker for CC-Jul8 than for Jul20 (Figure 8b compare dotted red and full

CHRISTENSEN ET AL. 7 of 15

21699011, 2024, 1, Downloaded from https://agupubs.onlinelibrary.wiley.com/doi/10.1029/2023JF007389 by Mbl Whoi Library, Wiley Online Library on [04/01/2024]. See the Terms

and-conditions) on Wiley Online Library for rules of use; OA articles are governed by the applicable Creative

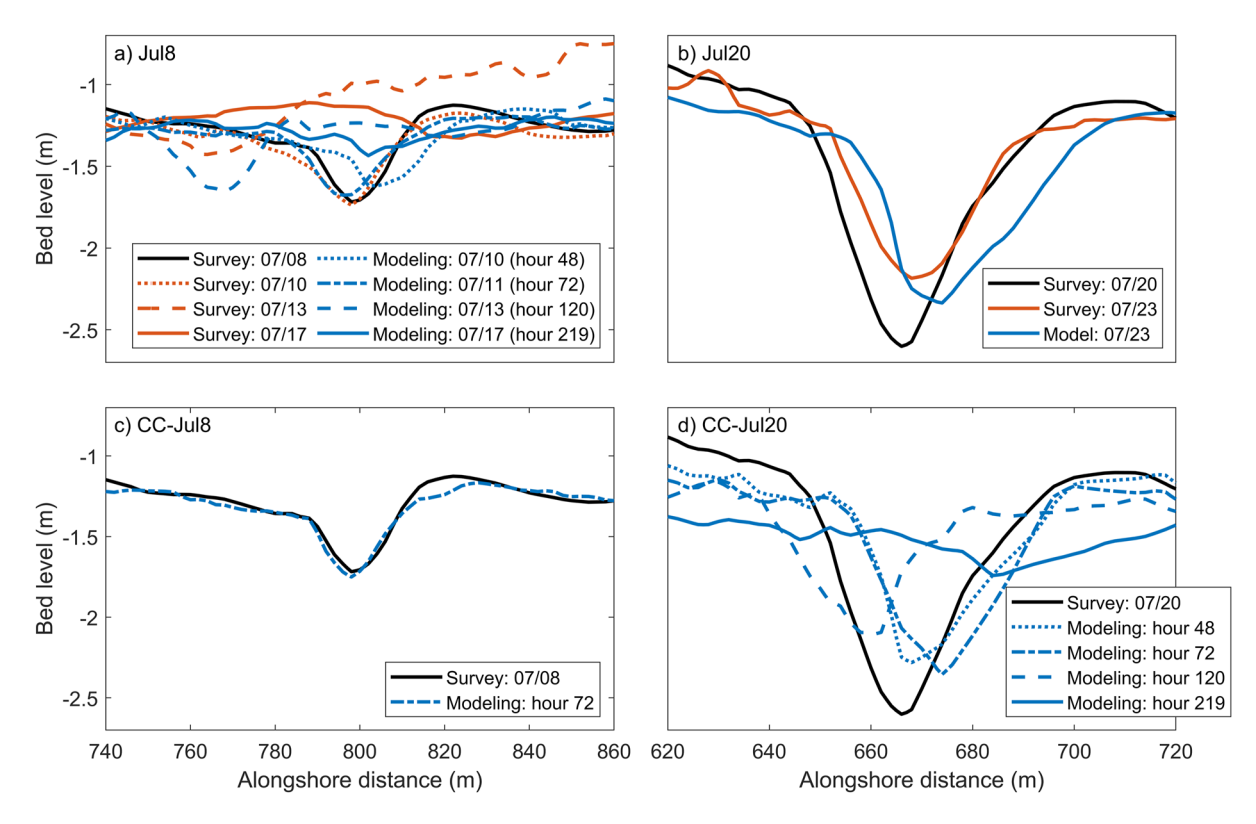
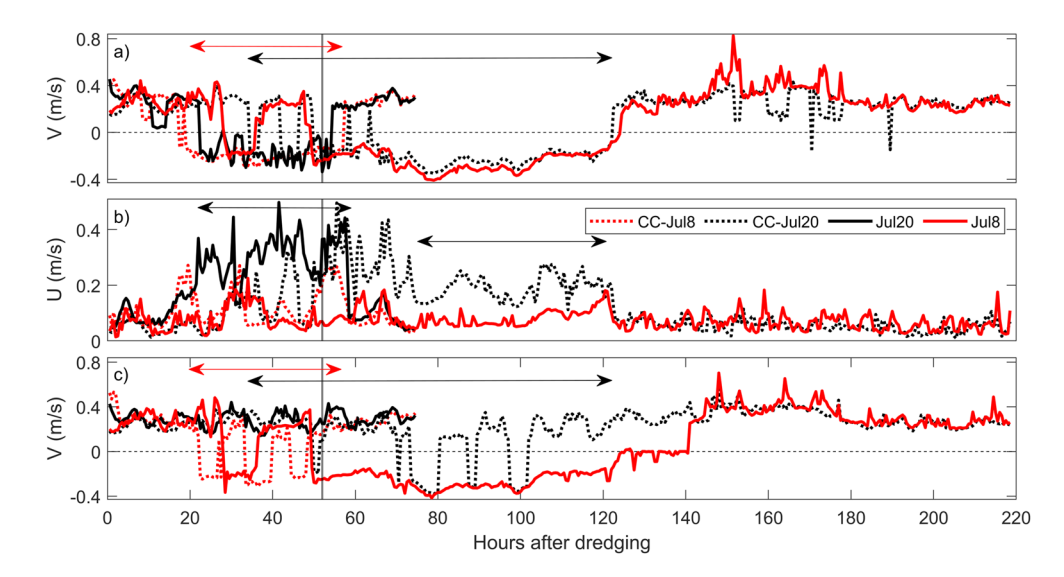


Figure 7. Bed level (depth relative to NAVD88) versus alongshore distance of initial (black), surveyed (orange), and modeled (blue) alongshore transects of bed levels during (a) Jul8, (b) Jul20, (c) CC-Jul8, and (d) CC-Jul20 near the channel midpoints at cross-shore coordinate 130 m (a, c) and 145 m (b, d).

black curves, and Table 1). On average, the rip current velocity during hours of converging feeders is 40% smaller during CC-Jul8 than during Jul20. The flows resulted only in minor morphological changes, as was also the case for Jul8 for hours 1–72 (Figures 7a and 7c, and Table 1).

Although in the field no rip current occurred after channel dredging on July 8, for CC-Jul20 (Jul20 bathymetry, Jul8 waves) there is flow convergence during low tides between hours 35 and 122 (Figures 8a and 8c see dotted



**Figure 8.** (a, c) Alongshore and (b) cross-shore modeled flows versus time (hours after channel dredging) for Jul8 (solid red), Jul20 (solid black), CC-Jul8 (dotted red), and CC-Jul20 (dotted black). The vertical dark gray bars are drawn at hour 52. The arrows highlight the time periods of interest.

CHRISTENSEN ET AL. 8 of 15

21699011, 2024, 1, Downloaded from https://agupubs.onlinelibrary.wiley.com/doi/10.1029/2023JF007389 by Mbl Whoi Library.

Table 1 Summary of the Simulation Results for Hours 1-72 Showing for the Four Cases (Jul8, Jul20, CC-Jul8, and CC-Jul20): Maximum Rip Current Velocity, Maximum Consecutive Hours of Rip Presence, Bed-Level Changes in the Channel Center, Alongshore Shift in Channel Position, and Cross-Sectional Volume Change

Hour 1-72	Jul8	Jul20	CC-Jul8	CC-Jul20
FLOWS				
Max. rip current velocity (m/s)	0	0.50	0.27	0.50
Max. consecutive hours of rip presence	0	32	9	21
MORPHOLOGY				
Channel center bed level changes (m, -erosion/+ deposition)	0.05	0.26	-0.03	0.25
Alongshore shift in channel position	0 m	8 m toward north	0 m	8 m toward north
Cross-sectional volume (m³/m) change (+gain/-loss)	2.0	5.4	1.9	2.9

black curve for the period highlighted by black arrows), and rip velocities up to 0.5 m/s (Figure 8b, dotted black curve, and Table 1) comparable with the Jul20 velocities (Figure 8b, compare dotted with solid black curves, and see Table 1). During the first 72 hr when a strong rip was present, the bathymetric evolution of CC-Jul20 followed the same trends as Jul 20 with deposition on the southern channel slope (between alongshore coordinate 650–670 m, Figures 7b and 7d) resulting in a northward channel displacement (Table 1), and decreasing channel depths (Table 1). These similar trends suggest that channel evolution depends on the initial channel dimension. The modeled channel infilling (Figure 7d) may cause the smaller CC-Jul20 rip velocities between hour 75 and 120 relative to the modeled and observed rip velocities between hours 24 and 60 during Jul 20 (Figure 8b, compare dotted with full black curves for periods highlighted by black arrows). For each of these two periods, the offshore mean wave directions were close to shore normal  $(70^{\circ} < \text{MWD} < 90^{\circ}, \text{Figure 4d})$ , whereas wave heights were larger during the CC-Jul20 (0.7  $< H_s > 1.7$  m, Figure 4b red curve) than during Jul20 (0.8  $< H_s > 1$  m, Figure 4b black curve). Thus, based on the wave conditions larger rip velocities were expected for CC-Jul20.

The weaker rip currents after hour 72 (Figure 8b) and dominating longshore currents after hour 122 resulted in alongshore channel migration where CC-Jul20 followed the migration trends of Jul8 (Figure 9). Hence, wave conditions are also important for channel evolution.

To examine rip generation in more detail, the individual terms of the momentum balance (Equation 1) for CC-Jul8 are compared with those from Jul20. During Jul20, nearshore (cross-shore coordinate 130 m) setup is small within the channel compared with that on the sides (Figure 10b, cyan curve), whereas the opposite is true for CC-Jul8 (Figure 10a). The setup (Figure 10b) also appears to increase at the point of flow convergence

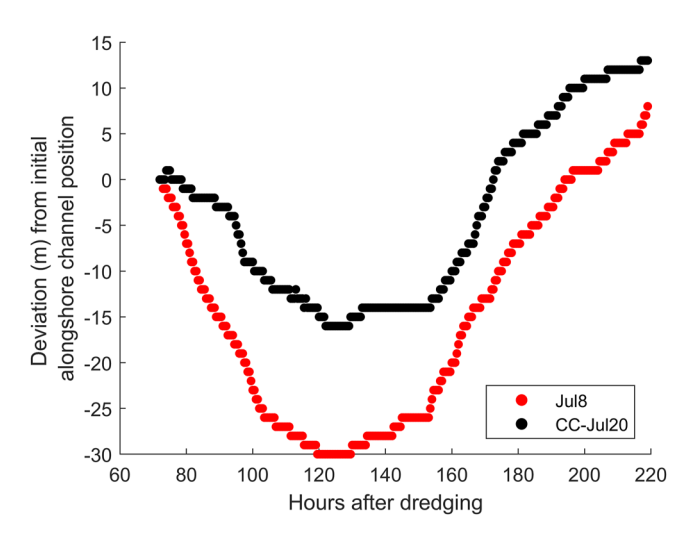


Figure 9. Simulated alongshore channel migration (-southwards, +northwards) during hours 72-219 for Jul8 (red) and CC-Jul20 (black).

(alongshore coordinate 665 m, Figure 11b), indicating that mean water levels are increased both by the cross-shore gradients in the cross-shore radiation stress component  $(\partial S_{xx}/\partial x)$  and by the convergence of the feeder currents. In other words, alongshore gradients in setup are not only forcing flows, but also are a result of the flows. Cross-shore and alongshore momentum balances are thereby linked, which complicates the patterns of the forcings, especially when examining setup during CC-Jul8 where alongshore setup variations are smaller (Figure 10a). Flow convergence near the alongshore coordinate 800 m (Figure 11a) causes a setup within the channel (Figure 10a) and a displacement of the local setup minimum to the south.

Rip current meandering (e.g., Figure 11b) might also affect the spatial variations in setup, with increases in water level owing to centrifugal forces in the curving flows. This effect is expected to be small compared with wave-driven setup. Significant wave heights are smaller north and south of the channel compared with those in the center due to the stronger wave breaking on the shallower sides (Figures 10a and 10b blue curves). However, for Jul20, wave heights have local maxima on the channel sides at alongshore coordinates 655 and 685 m, and a local minimum in the center at 670 m (Figure 10b). The focusing of the wave energy on the channel sides is a result of wave refraction

CHRISTENSEN ET AL. 9 of 15

21699011, 2024, 1, Downloaded from https://agupubs.onlinelibrary.wiky.com/doi/10.1029/2023JF007389 by Mbl Whoi Library. Wiley Online

Library on [04/01/2024]. See the Terms and Conditions (https://onlinelibrary.wiley.com/terms-and-conditions) on Wiley Online Library for rules of use; OA articles are governed by the applicable Creative Commons Licens

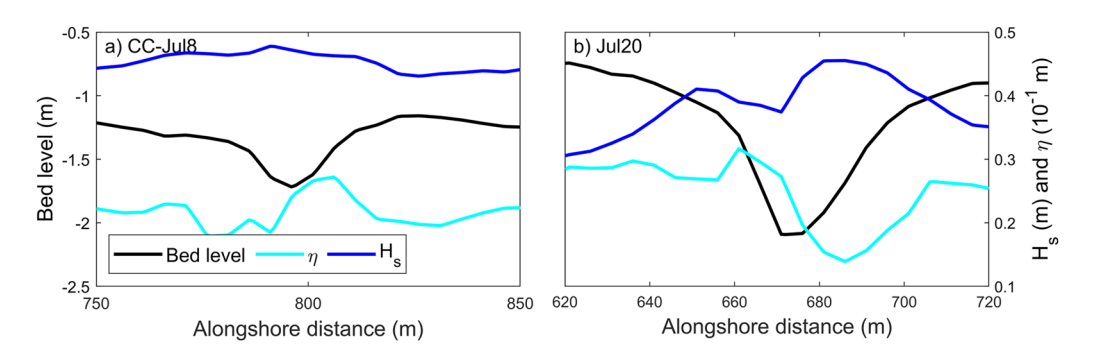


**Figure 10.** Bed level (depth relative to NAVD88, black curves, left-hand axes) and significant wave height ( $H_s$ , blue curves, right-hand axes) and setup ( $\eta$ , cyan curves, right-hand axes) versus alongshore distance for (a) CC-Jul8 and (b) Jul20 52 hr after channel dredging near the channel midpoint at cross-shore coordinate 130 m.

over the channel and contributes to forcing a flow toward the center, even though the forcings are up to a factor 10 smaller than the forcing from alongshore setup gradients  $(gh \cdot \partial \eta/\partial y)$ , Figure 12b compare blue with red curves, positive gradients pose a force toward the south, whereas negative gradients pose a force toward the north).

Prior modeling of the Jul20 case (Moulton et al., 2017) showed local maxima of the vortex forcing on the channel sides, consistent with the wave energy and  $\partial S_{yy}/\partial y$  forcing seen here. During CC-Jul8,  $\partial S_{yy}/\partial y$  (and advection) is insignificant (green, purple, and cyan curves in Figure 12a) and setup gradients  $(gh \cdot \partial \eta/\partial y)$ , red curve in Figure 12a) are the main forcing term. Convergence occurs near alongshore coordinate 790 m (the region of converging flows indicated by red arrows in Figure 12c) coincident with the rip flow (Figure 11a cross-shore distance 130 m). During Jul20, the advection is significant and acts in the opposite direction of the setup gradients

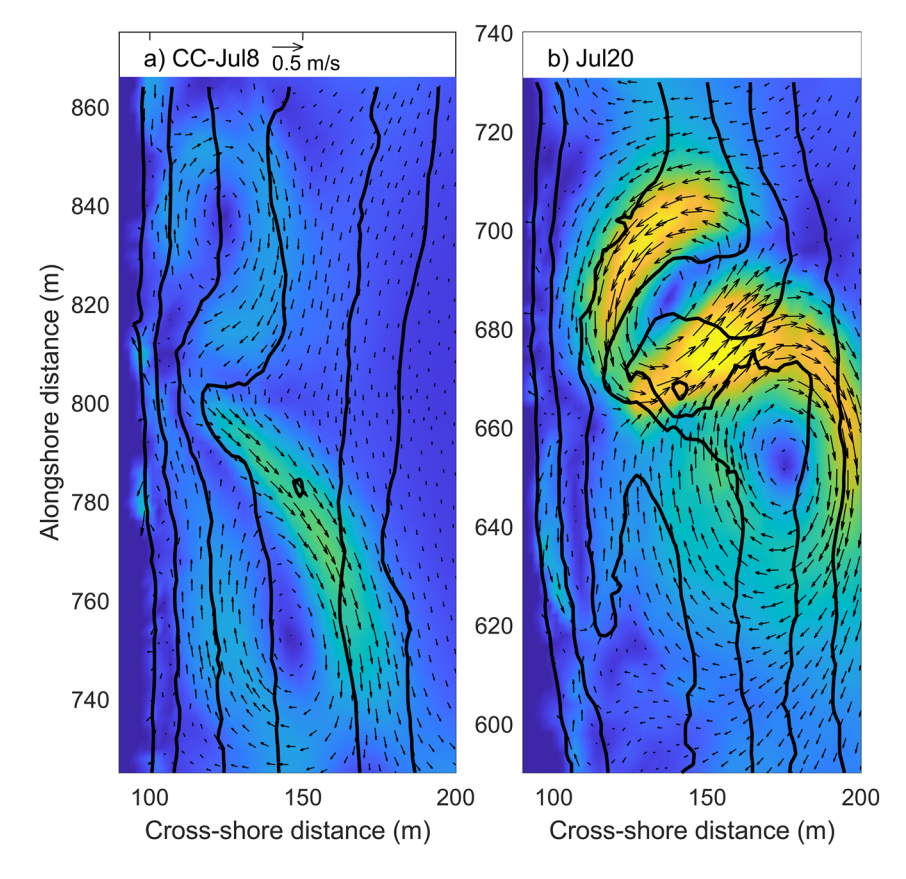


Figure 11. Simulated ½-hour averaged flows (arrows point in direction of flow with length proportional to speed) during hour 52 for (a) CC-Jul8, and (b) Jul20. Black curves represent depth contours every 0.5 m and color contours are velocity magnitudes.

CHRISTENSEN ET AL. 10 of 15

21699011, 2024, 1, Downloaded from https://agupubs.onlinelibrary.wiley.com/doi/10.1029/2023JF007389 by Mbl Whoi Library. Wiley Online Library on [04/01/2024]. See the Terms and Con

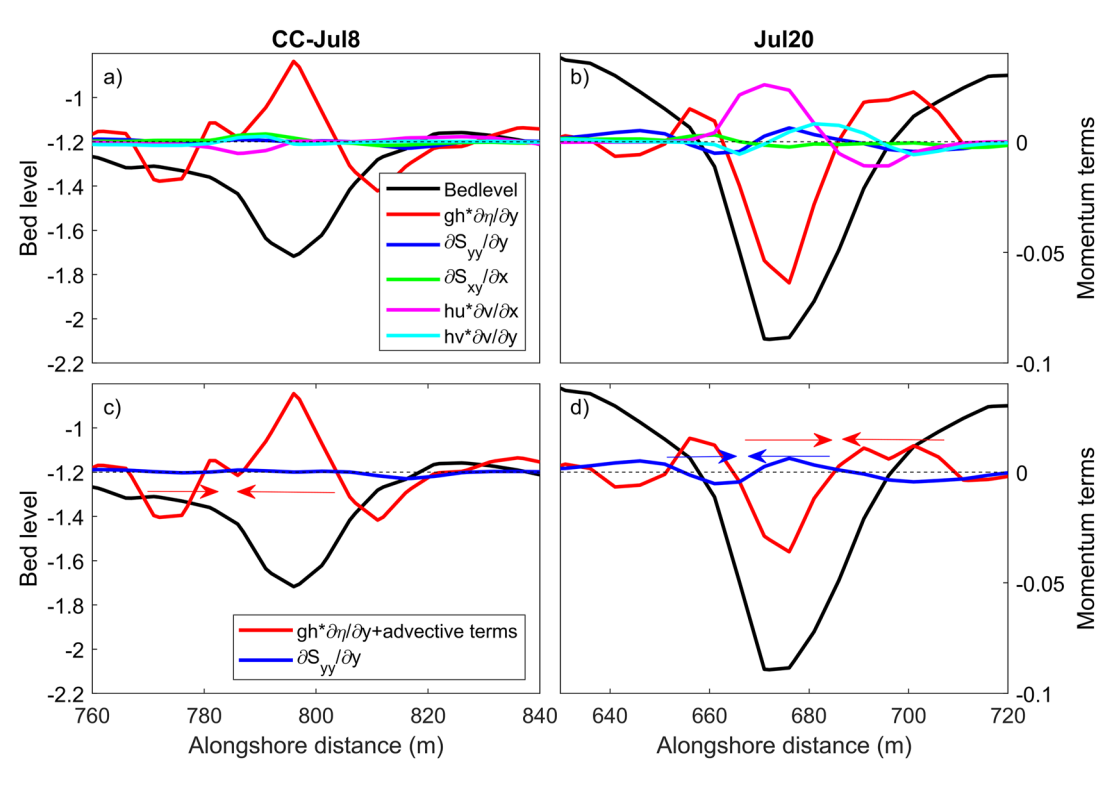
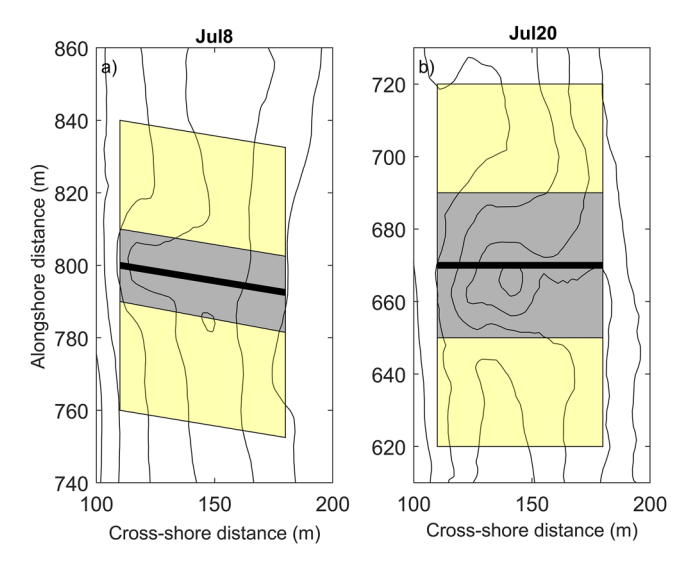


Figure 12. Bed level (depth relative to NAVD88, black curves, left-hand axes) and with right-hand axes  $gh \cdot \partial \eta/\partial y$  (red),  $\partial S_{xy}/\partial x$  (green),  $hu \cdot \partial v/\partial x$  (magenta), and  $hv \cdot \partial v/\partial y$  (cyan) versus alongshore distance for (a) CC-Jul8 and (b) Jul20, and bed level (black curves, left-hand axes) and with right-hand axes  $gh \cdot \partial \eta/\partial y + hu \cdot \partial v/\partial x + hv \cdot \partial v/\partial y$  (red), and  $\partial S_{xy}/\partial y$  (blue) for (c) CC-Jul8 and (d) Jul20 52 hr after channel dredging near the channel midpoint at cross-shore coordinate 130 m. Arrows in (c and d) show force convergences.



**Figure 13.** Rectangles defining the alongshore and cross-shore areas within forcing terms are averaged. Gray rectangles indicate the channel areas and yellow rectangles the northern and southern side areas for (a) Jul8 bathymetry with channel areas defined as channel center (alongshore coordinate 793–800 m)  $\pm$  10 m, and outer areas defined as channel area limits  $\pm$  30 m, and (b) Jul20 bathymetry with channel areas defined as channel center (alongshore coordinate 670 m)  $\pm$  20 m, and outer areas defined as channel area limits  $\pm$  30 m. In the cross-shore, the rectangles cover 70 m from cross-shore coordinate 110–180 m.

(compare magenta and cyan curves with the red curve in Figure 12b), thereby reducing the dominance of the setup gradients in driving the rip currents (compare red curve in Figure 12d with that in Figure 12b). The  $\partial S_{yy}/\partial y$  term (blue curve in Figure 12d) is significant (up to 20% of the total forcing) and can shift the forcing for the feeder currents in the alongshore direction (see the region of converging forces indicated by red and blue arrows in Figure 12d). During both Jul20 and CC-Jul8, the third term of the momentum balance,  $\partial S_{xy}/\partial x$  is small and causes flow divergence in the channel (green curves in Figures 12a and 12b).

Comparison of the forcing terms for hour 52 for CC-Jul8 with those for Jul20 indicates that the channel dimensions affect the rip current strength by influencing not only the magnitude of setup gradients  $(\partial \eta/\partial y)$  but also of  $\partial S_{yy}/\partial y$  through wave refraction and energy convergence (divergence) on the channel sides (center). To examine the forcing mechanisms throughout the experiments, spatial averages of terms are calculated within the channel and on the channel sides (Figure 13).

Alongshore setup gradients  $(\partial \eta/\partial y)$  and advection drive converging flows toward the channel sides (yellow regions in Figure 13b) from hour 22 to 55 during Jul20 (Figure 14a, solid black curve mostly is positive and the dashed black curve mostly is negative for the period highlighted by the black arrow), corresponding to the period of observed rip currents, whereas  $\partial S_{yy}/\partial y$  partially balances this forcing (Figure 14b, solid black curve mostly is negative and dashed black curve mostly is positive). Within the channel center for Jul20 (gray regions in Figure 13b), the setup forcing  $(gh \cdot \partial \eta/\partial y)$  and advection primarily drive diverging flows that are partially balanced by

CHRISTENSEN ET AL. 11 of 15

21699011, 2024, 1, Downloaded from https://agupubs.onlinelibrary.wiley.com/doi/10.1029/2023JR007389 by Mbl Whoi Library, Wiley Online Library on [04/01/2024]. See the Terms and Conditional Condition

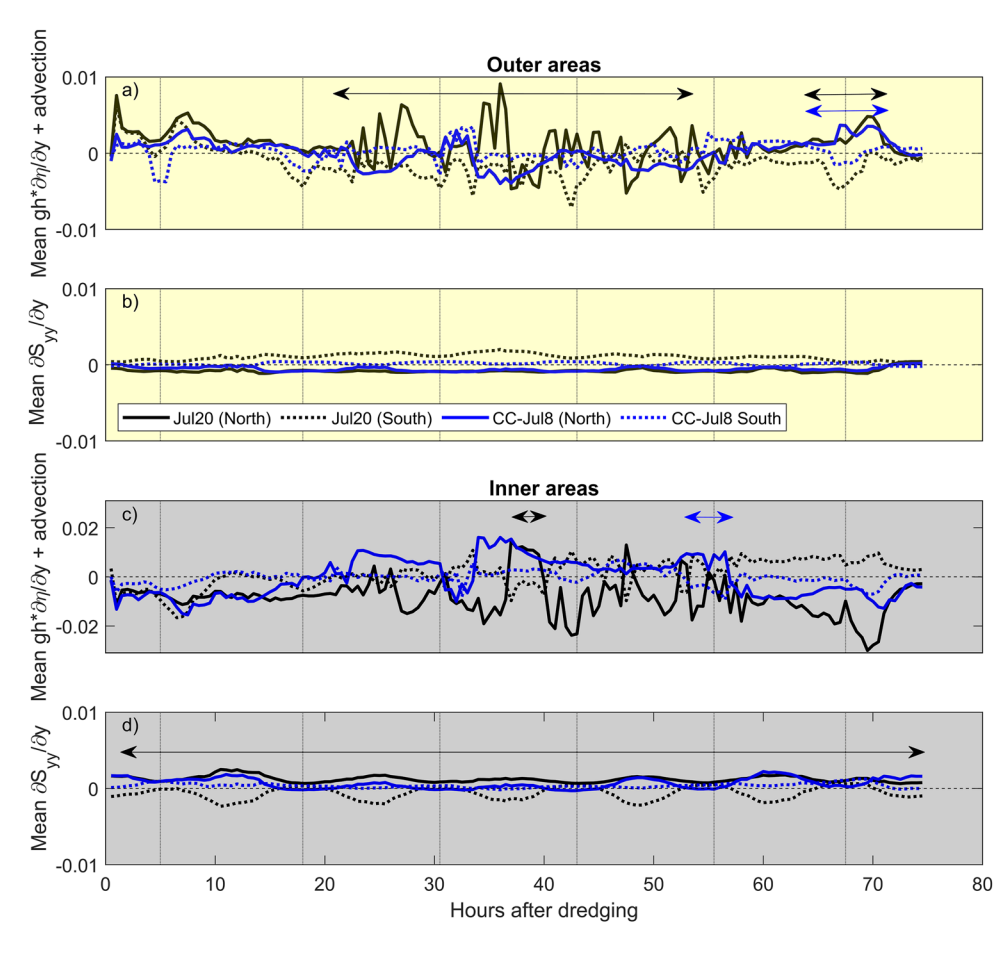


**Figure 14.** Average (a, c)  $gh \cdot \partial \eta/\partial y$  + advection and (b, d)  $\partial S_{yy}/\partial y$  north (solid curves) and south (dashed curves) versus time (hours since dredging) for the CC-Jul8 (blue) and Jul20 (black) channels. The thin vertical gray lines are drawn at low tides. The black (blue) arrows indicate the hours of convergence in the forcing terms for Jul20 (CC-Jul8).

convergent forcing from  $\partial S_{yy}/\partial y$  (especially at high tide) with strong convergence from all forcing terms limited to hours 36 to 41 (Figures 14c and 14d convergence shown by positive solid black curves, and negative dashed black curves, hour 36–41 highlighted by black arrow). In contrast, for CC-Jul8, the forcing outside the channel is typically unidirectional or divergent (Figures 14a and 14b, divergence shown by positive dashed blue curves and, and negative solid blue curves) except between hour 63 to 70 where convergent forcing occurs for both cases (Figure 14a, period highlighted by black and blue arrows), but no rip was present (not shown). However, within the channel center, setup gradients  $(\partial \eta/\partial y)$  and advection drive convergence during the period of the strongest rip current velocities (hour 53–57, Figure 14c period highlighted by blue arrow). Unlike Jul20, forcings from  $\partial S_{yy}/\partial y$  are mostly unidirectional and only converging when magnitudes are insignificant (Figure 14d).

During Jul20 and CC-Jul20, which had a deeper and longer channel, alongshore setup gradients primarily are toward the channel sides (forcings occurring 58% and 36% of the time, respectively), whereas for the Jul8-bathymetry alongshore setup gradients toward the channel side (15% of the time) and channel center (16% of the time) occur for similar time periods, with the largest gradients within the confined area close to the channel center (Table 2). Whereas  $\partial S_{yy}/\partial y$  contributes to driving a flow toward the channel center for Jul20 and CC-Jul20,  $\partial S_{yy}/\partial y$  is insignificant for CC-Jul8. The similarities between the Jul20 and CC-Jul20 results (and between Jul8 and CC-Jul8) suggest that the spatial distribution of rip current forcings and the relative importance of terms depend on the channel geometry.

CHRISTENSEN ET AL. 12 of 15

**Table 2**Summary of the Simulated Forcing Conditions for Hour 1–72 Showing for the Four Cases (Jul8, Jul20, CC-Jul8, and CC-Jul20): Time-Averaged  $gh \cdot \partial \eta/\partial y + Advection$  and  $\partial S_{yy}/\partial y$  Within the Channels (Inner) and on the Channel Sides (Outer) for Hours of Force Convergence

Hour 1-72		Jul8	Jul20	CC-Jul8	CC-Jul20
FORCINGS	Areas				
Average $(gh \cdot \partial \eta/\partial y + \text{advection})$ (m <sup>2</sup> /s <sup>2</sup> ) during hours of force-convergence and percentage of occurrence	Outer	-	0.002 (58%)	0.001 (15%)	0.002 (36%)
	Inner	-	0.006 (10%)	0.004 (16%)	0.011 (16%)
Average $\partial S_{yy}/\partial y$ (m <sup>2</sup> /s <sup>2</sup> ) during hours of force-convergence and percentage of occurrence	Outer	-	(0%)	$0.000^{a}$ (3%)	(0%)
	Inner	-	0.001 (69%)	0.000° (6%)	0.001 (63%)

Note. In parentheses are the percentages of force-convergence occurrence.

#### 5. Discussion

## 5.1. Forcing Mechanisms and Implications for Rip Channel Spacing

The field-verified model suggests that both alongshore gradients in setup  $(\partial \eta/\partial y)$  and  $\partial S_{yy}/\partial y$  contribute to driving the converging feeder currents and thus rips. For the short, shallow channel (Jul8 and CC-Jul8), alongshore gradients in setup dominate the forcing of the feeder currents. For the deeper, longer channel (Jul20 and CC-Jul20), wave refraction and focusing results in  $\partial S_{yy}/\partial y$  forcing from the channel sides to the center, consistent with prior studies (Kumar et al., 2011). Assuming depth-limited wave heights, the relative importance of setup  $(\partial \eta/\partial y)$  and  $\partial S_{yy}/\partial y$  is expected to depend on the alongshore bed slope (MacMahan et al., 2006), which is similar (roughly 0.03) for both channels. However, prior results at this field site suggest that the flows can be reproduced reasonably well considering only processes affecting the setup (Moulton et al., 2017). For a channel incising a relatively deep sandbar, wave breaking was reduced in the rip channel, resulting in  $\partial S_{yy}/\partial y$  with the opposite sign to the setup gradient, causing a reduced magnitude of the feeder currents (Haller et al., 2002). Here, for channels crossing a shallow terrace and bar, the channel geometry is shown to control the relative importance of  $\partial \eta/\partial y$  and  $\partial S_{yy}/\partial y$  to forcing feeder flows.

Alongshore gradients in the setup are less affected by wave refraction and focusing because the setup depends only on the normal component of the radiation stresses, which have minimal variations for small deviations from normal incidence. Thus, the relative contribution from each term varies with the channel and nearshore bathymetry, which may have implications for the morphological evolution and the stability of channel spacing in multiple rip systems. For example, spatial variations in setup occur over larger alongshore distances (from outside the channel toward the channel) than do variations in  $S_{yy}$ , and thus rip channel spacing could be smaller for systems driven primarily by  $\partial S_{yy}/\partial y$ , than for cases driven primarily by alongshore setup gradients.

#### 5.2. Channel Dimensions

The MIKE21 simulations successfully reproduced the trends in channel evolution during the two experiments, and in accordance with previous field observations (Short, 1985) for oblique incident waves, channel rips migrate in the direction of the mean current and fill in. However, the threshold for when an alongshore current driven by oblique waves overwhelms rip current generation is dependent on the channel dimensions. During CC-Jul20 (i.e., Jul20 bathymetry with Jul8 waves), a rip current was present (e.g., hour 42–46, Figure 8) during stronger oblique wave forcing (Figure 4d: 135° < MWD < 144° for hour 42–46) than for Jul8. In addition, for the same wave conditions, the Jul8 bathymetry did not result in rip generation, whereas the Jul20 bathymetry resulted in rip current generation during a large range of tidal water levels. These results highlight that rip generation is related not only to the wave conditions and the water levels but also to the channel dimensions, consistent with prior studies (Calvete et al., 2007; McCarroll et al., 2018). The different flow conditions shown here for terrace (Jul8) and bar (Jul20) bathymetry highlights the need for more experiments conducted on more planar beaches to examine further rip current sensitivity to bathymetric variability under a range of wave conditions.

### 6. Conclusions

Simulations conducted with MIKE21 reproduced observed trends in flows and bathymetric evolution for two channels dredged across a nearshore sandbar and terrace on an Atlantic Ocean beach near Duck, NC, USA. In one

CHRISTENSEN ET AL. 13 of 15

<sup>&</sup>lt;sup>a</sup>Values are smaller than 0.0005.



## **Journal of Geophysical Research: Earth Surface**

case, a strong rip current was driven by moderate height near-normal incidence waves in a channel with relatively little bathymetric evolution. The other case was characterized by 2 days of oblique waves and alongshore flows during which the channel incurred little change, followed by a southward migration of the channel and infilling during more normally incident, but larger waves. Model simulations conducted with the channel geometries for cases 1 and 2 but with the waves from cases 2 and 1, respectively suggest that the different bathymetries were the dominant factor controlling the flows. Hence, rip generation was most similar for cases with the same initial bathymetry, irrespective of the wave conditions. On the other hand, both initial morphology and wave conditions were important for the channel evolution. Rip currents were primarily forced by alongshore setup gradients driving converging feeder currents. However, over the deeper and longer channel incising a nearshore bar, alongshore gradients in the alongshore component of the radiation stress tensor that result from alongshore variations in wave dissipation, shoaling, and refraction modulated the strength of the feeders and affected the spatial distribution of rip current forcings.

## **Data Availability Statement**

Field data collected at the US Army Corps of Engineers Field Research Facility (FRF) on the Outer Banks, near Duck, NC, USA between 8 July and 24 July 2012 were used in the creation of this manuscript. These velocity, pressure, and bathymetry data are available at https://doi.org/10.17603/ds2-t76g-p598 (Elgar et al., 2023). Data on offshore wave conditions and bathymetry on the FRF site were downloaded from the CHL Data Server (https://chlthredds.erdc.dren.mil/thredds/catalog/frf/catalog.html). Model simulations were performed in the software package MIKE21 (version 2020), and the output files needed to evaluate or reproduce the results are available at https://doi.org/10.17894/ucph.d534cffa-35cb-46e4-8579-6212d98c4872 (Christensen et al., 2023). Field data processing and figures were made in MATLAB R2021a.

#### Acknowledgments

We thank Dr. Melissa Moulton for help planning and executing the dredging experiments and for many years of useful discussions, Jason Pipes and Brian Scarborough for their expert piloting of the landing craft used to dredge the channels, and the US Army Corps of Engineers Field Research Facility and the PVLAB field crews for excellent field support in sometimes difficult conditions. We also thank DHI for the use of their MIKE21 software, and Aart Kroon for insightful comments on the manuscript. Funding was provided by the Villum Foundation, a Vannevar Bush Faculty Fellowship, and the US National Science Foundation.

#### References

- Aagaard, T., Greenwood, B., & Nielsen, J. (1997). Mean currents and sediment transport in a rip channel. Marine Geology, 140(1-2), 25-45. https://doi.org/10.1016/S0025-3227(97)00025-X
- Badru, G. S., Odunuga, S. S., Omoiola, A. S., & Oladipo, E. O. (2022). Numerical modelling of sediment transport in southwest coast of Nigeria; Implications for sustainable management of coastal erosion in the Bight of Benin. Journal of African Earth Sciences, 187, 104466. https://doi. org/10.1016/j.jafrearsci.2022.104466
- Brander, R. W. (1999). Field observations on the morphodynamic evolution of a low-energy rip current system. Marine Geology, 157(3-4), 199-217. https://doi.org/10.1016/S0025-3227(98)00152-2
- Brander, R. W. (2015). Rip currents. In Coastal and marine hazards, risks, and disasters (pp. 335-379). Elsevier. https://doi.org/10.1016/ B978-0-12-396483-0.00012-1
- Brown, J., MacMahan, J., Reniers, A., & Thornton, E. (2009). Surf zone diffusivity on a rip-channeled beach. Journal of Geophysical Research, 114(C11), C11015. https://doi.org/10.1029/2008JC005158
- Brown, J. A., MacMahan, J. H., Reniers, A. J. H. M., & Thornton, E. B. (2015). Field observations of surf zone-inner shelf exchange on a  $rip-channeled\ beach.\ \textit{Journal\ of\ Physical\ Oceanography},\ 45 (9),\ 2339-2355.\ https://doi.org/10.1175/JPO-D-14-0118.1$
- Bruneau, N., Bonneton, P., Castelle, B., & Pedreros, R. (2011). Modeling rip current circulations and vorticity in a high-energy mesotidal-macrotidal environment. Journal of Geophysical Research, 116(C7), 2010JC006693. https://doi.org/10.1029/2010JC006693
- Cáceres, R. A., Zyserman, J. A., & Perillo, G. M. E. (2016). Analysis of Sedimentation Problems at the Entrance to Mar del Plata Harbor. Journal of Coastal Research, 32(2), 301. https://doi.org/10.2112/JCOASTRES-D-14-00056.1
- Calvete, D., Coco, G., Falqués, A., & Dodd, N. (2007). (Un)predictability in rip channel systems. Geophysical Research Letters, 34(5), L05605. https://doi.org/10.1029/2006GL028162
- Calvete, D., Dodd, N., Falqués, A., & van Leeuwen, S. M. (2005). Morphological development of rip channel systems: Normal and near-normal
- wave incidence. Journal of Geophysical Research, 110(C10), C10006. https://doi.org/10.1029/2004JC002803 Castelle, B., Michallet, H., Marieu, V., Leckler, F., Dubardier, B., Lambert, A., et al. (2010). Laboratory experiment on rip current circulations over
- a moveable bed: Drifter measurements. Journal of Geophysical Research, 115(C12), 2010JC006343. https://doi.org/10.1029/2010JC006343 Christensen, D. F., Raubenheimer, B., & Elgar, S. (2023). MIKE21 simulation outputs—The BARGAP experiment [Dataset]. UCPH. https://doi. org/10.17894/ucph.d534cffa-35cb-46e4-8579-6212d98c4872
- Dalrymple, R. A., MacMahan, J. H., Reniers, A. J. H. M., & Nelko, V. (2010). Rip currents. Annual Review of Fluid Mechanics.
- Damgaard, J., Dodd, N., Hall, L., & Chesher, T. (2002). Morphodynamic modelling of rip channel growth. Coastal Engineering, 45(3-4), 199-221. https://doi.org/10.1016/S0378-3839(02)00034-0
- Deigaard, R., Drønen, N., Fredsøe, J., Jensen, J. H., & Jørgensen, M. P. (1999). A morphological stability analysis for a long straight barred coast. Coastal Engineering, 36(3), 171-195. https://doi.org/10.1016/S0378-3839(99)00005-8
- DHI. (2017a). MIKE 21 flow model & MIKE 21 flood screening tool—Hydrodynamic module. DHI Group.
- DHI. (2017b). MIKE 21—Spectral wave module—Scientific documentation. DHI Group.
- DHI. (2020). MIKE 21 & MIKE 3 flow model FM Sand transport module—Scientific documentation. DHI Group.
- Elgar, S., Raubenheimer, B., & Moulton, M. (2023). BARGAP: Waves, currents, and bathymetry near dredged channels in the surfzone seafloor [Dataset]. DesignSafe-CI. https://doi.org/10.17603/ds2-t76g-p598
- Fujimura, A. G., Reniers, A. J. H. M., Paris, C. B., Shanks, A. L., MacMahan, J. H., & Morgan, S. G. (2014), Numerical simulations of larval transport into a rip-channeled surf zone. Limnology & Oceanography, 59(4), 1434-1447. https://doi.org/10.4319/lo.2014.59.4.1434

CHRISTENSEN ET AL. 14 of 15

- Gallop, S. L., Bryan, K. R., Pitman, S. J., Ranasinghe, R., Sandwell, D. R., & Harrison, S. R. (2018). Rip current circulation and surf zone retention on a double barred beach. *Marine Geology*, 405, 12–22. https://doi.org/10.1016/j.margeo.2018.07.015
- Haas, K. A., & Svendsen, I. A. (2002). Laboratory measurements of the vertical structure of rip currents. *Journal of Geophysical Research*, 107(C5), 3047. https://doi.org/10.1029/2001JC000911
- Haller, M. C., Dalrymple, R. A., & Svendsen, I. A. (2002). Experimental study of nearshore dynamics on a barred beach with rip channels. *Journal of Geophysical Research*, 107(C6), 3061. https://doi.org/10.1029/2001JC000955
- Holthuijsen, L. H., Booij, N., & Herbers, T. H. C. (1989). A prediction model for stationary, short-crested waves in shallow water with ambient currents. Coastal Engineering, 13(1), 23–54. https://doi.org/10.1016/0378-3839(89)90031-8
- Hong, X., Zhang, Y., Wang, B., Zhou, S., Yu, S., & Zhang, J. (2021). Numerical study of rip currents interlaced with multichannel sandbars. Natural Hazards, 108(1), 593–605. https://doi.org/10.1007/s11069-021-04696-8
- Houser, C., Wernette, P., Trimble, S., & Locknick, S. (2020). Rip currents. In Sandy beach morphodynamics (pp. 255–276). Elsevier. https://doi.org/10.1016/B978-0-08-102927-5.00011-4
- Hu, P., Li, Z., Zhu, D., Zeng, C., Liu, R., Chen, Z., & Su, Q. (2022). Field observation and numerical analysis of rip currents at Ten-Mile Beach, Hailing Island, China. Estuarine, Coastal and Shelf Science, 276, 108014. https://doi.org/10.1016/j.ecss.2022.108014
- Kennedy, A. B., & Thomas, D. (2004). Drifter measurements in a laboratory rip current. *Journal of Geophysical Research*, 109(C8), C08005. https://doi.org/10.1029/2003JC001927
- Kennedy, A. B., Zhang, Y., & Haas, K. A. (2008). Rip currents with varying gap widths. Journal of Waterway, Port, Coastal, and Ocean Engineering, 134(1), 61–65. https://doi.org/10.1061/(ASCE)0733-950X(2008)134:1(61)
- Komen, G. J., Cavaleri, L., Doneland, M., Hasselmann, K., Hasselmann, S., & Janssen, P. A. E. M. (1994). Dynamics and modelling of ocean
- Kumar, N., Voulgaris, G., & Warner, J. C. (2011). Implementation and modification of a three-dimensional radiation stress formulation for surf
- zone and rip-current applications. Coastal Engineering, 58(12), 1097–1117. https://doi.org/10.1016/j.coastaleng.2011.06.009

  MacMahan, J., Brown, J., Brown, J., Thornton, E., Reniers, A., Stanton, T., et al. (2010). Mean Lagrangian flow behavior on an open coast
- rip-channeled beach: A new perspective. *Marine Geology*, 268(1–4), 1–15. https://doi.org/10.1016/j.margeo.2009.09.011 MacMahan, J. H., Thornton, E. B., & Reniers, A. J. H. M. (2006). Rip current review. *Coastal Engineering*, 53(2–3), 191–208. https://doi.
- org/10.1016/j.coastaleng.2005.10.009
  Marchesiello, P., Benshila, R., Almar, R., Uchiyama, Y., McWilliams, J. C., & Shchepetkin, A. (2015). On tridimensional rip current modeling.
- Marchestello, P., Benshila, R., Almar, R., Uchiyama, Y., McWilliams, J. C., & Shchepetkin, A. (2015). On tridimensional rip current modeling Ocean Modelling, 96, 36–48. https://doi.org/10.1016/j.ocemod.2015.07.003
- McCarroll, R. J., Brander, R. W., Scott, T., & Castelle, B. (2018). Bathymetric controls on rotational surfzone currents. *Journal of Geophysical Research: Earth Surface*, 123(6), 1295–1316. https://doi.org/10.1029/2017JF004491
- Moulton, M., Elgar, S., & Raubenheimer, B. (2014). Improving the time resolution of surfzone bathymetry using in situ altimeters. *Ocean Dynamics*, 64(5), 755–770, https://doi.org/10.1007/s10236-014-0715-8
- Moulton, M., Elgar, S., Raubenheimer, B., Warner, J. C., & Kumar, N. (2017). Rip currents and alongshore flows in single channels dredged in the surf zone. *Journal of Geophysical Research: Oceans*, 122(5), 3799–3816. https://doi.org/10.1002/2016JC012222
- OCM Partners. (2023). 2016 coastal North Carolina NAIP digital ortho photo imagery (gov. noaa.nmfs.inport:49531) [Dataset]. OCM Partners. Retrieved from https://www.fisheries.noaa.gov/inport/item/49531
- Osorio-Cano, J. D., Alcérreca-Huerta, J. C., Mariño-Tapia, I., Osorio, A. F., Acevedo-Ramírez, C., Enriquez, C., et al. (2019). Effects of roughness loss on reef hydrodynamics and coastal protection: Approaches in Latin America. *Estuaries and Coasts*, 42(7), 1742–1760. https://doi.org/10.1007/s12237-019-00584-4
- Petropoulos, A., Kapsimalis, V., Evelpidou, N., Karkani, A., & Giannikopoulou, K. (2022). Simulation of the nearshore sediment transport pattern and beach morphodynamics in the semi-enclosed Bay of Myrtos, Cephalonia Island, Ionian Sea. *Journal of Marine Science and Engineering*, 10(8), 1015. https://doi.org/10.3390/jmse10081015
- Reniers, A. J. H. M., MacMahan, J. H., Thornton, E. B., Stanton, T. P., Henriquez, M., Brown, J. W., et al. (2009). Surf zone surface retention on a rip-channeled beach. *Journal of Geophysical Research*, 114(C10), C10010. https://doi.org/10.1029/2008JC005153
- Reniers, A. J. H. M., Roelvink, J. A., & Thornton, E. B. (2004). Morphodynamic modeling of an embayed beach under wave group forcing. Journal of Geophysical Research, 109(C1), C01030, https://doi.org/10.1029/2002JC001586
- Schmidt, W. E., Guza, R. T., & Slinn, D. N. (2005). Surf zone currents over irregular bathymetry: Drifter observations and numerical simulations. Journal of Geophysical Research, 110(C12), C12015. https://doi.org/10.1029/2004JC002421
- Shepard, F. P. (1936). Undertow, rip tide, or "rip current.". Science, 84(2173), 181-182. https://doi.org/10.1126/science.84.2173.181
- Short, A. D. (1985). Rip-current type, spacing and persistence, Narrabeen beach, Australia. Marine Geology, 65(1-2), 47-71. https://doi.org/10.1016/0025-3227(85)90046-5
- Valipour, A., & Bidokhti, A. A. (2018). An analytical model for the prediction of rip spacing in intermediate beaches. *Journal of Earth System Science*, 127(8), 108. https://doi.org/10.1007/s12040-018-1013-5
- Valipour, A., Khaniki, A. K., & Bidokhti, A. A. (2014). Investigating the reactions of rip current pattern and sediment transport in rip channel against changes of bed parameters using numerical simulations. *Indian Journal of Geo-Marine Sciences*, 43(5), 831–840.
- Warren, I. R., & Bach, H. (1992). MIKE21: A modelling system for estuaries, coastal waters and seas. *Environmental Software*, 7(4), 229–240. https://doi.org/10.1016/0266-9838(92)90006-p
- Winter, G. (2012). Rip current observations at Egmond aan zee. NCK-days 2012: Crossing borders in coastal research: Jubilee conference proceedings. NCK-days 2012: Crossing borders in coastal research. https://doi.org/10.3990/2.206
- Winter, G., Van Dongeren, A. R., De Schipper, M. A., & Van Thiel De Vries, J. S. M. (2014). Rip currents under obliquely incident wind waves and tidal longshore currents. Coastal Engineering, 89, 106–119. https://doi.org/10.1016/j.coastaleng.2014.04.001
- Wright, L. D., & Short, A. D. (1984). Morphodynamic variability of surf zones and beaches: A synthesis. Marine Geology, 56(1-4), 93-118. https://doi.org/10.1016/0025-3227(84)90008-2
- Zhang, Y., Shi, F., Kirby, J. T., & Feng, X. (2022). Phase-resolved modeling of wave interference and its effects on nearshore circulation in a large Ebb Shoal-beach system. *Journal of Geophysical Research: Oceans*, 127(10), e2022JC018623. https://doi.org/10.1029/2022JC018623

CHRISTENSEN ET AL. 15 of 15